Geophys. J. Int. (1998) **133,** 756–772

Inversion for interface structure using teleseismic traveltime residuals

N. Rawlinson[1] and G. A. Houseman[2]

[1] *Australian Geodynamics Cooperative Research Centre and Department of Earth Sciences, Monash University, Clayton, Victoria* 3168, *Australia*
[2] *Department of Earth Sciences, Monash University, Clayton, Victoria* 3168, *Australia*

Accepted 1997 December 18. Received 1997 December 9; in original form 1997 June 30

SUMMARY

An inversion method is presented for the reconstruction of interface geometry between two or more crustal layers from teleseismic traveltime residuals. The method is applied to 2-D models consisting of continuous interfaces separating constant-velocity layers. The forward problem of determining ray paths and traveltimes between incident wave fronts below the structure and receivers located on the Earth's surface is solved by an efficient and robust shooting method. A conjugate gradient method is employed to solve the inverse problem of minimizing a least-squares type objective function based on the difference between observed and calculated traveltimes. Teleseismic data do not accurately constrain average vertical structure, so *a priori* information in the form of layer velocities and average layer thicknesses is required. Synthetic tests show that the method can be used to reconstruct interface geometry accurately, even in the presence of data noise. Tests also show that, if layer velocities and initial interface positions are poorly chosen, lateral structure is still recoverable. The inversion method was applied to previously published teleseismic data recorded by an in-line array of portable seismographs that traversed the northern margin of the Musgrave Block, central Australia. The solution based on interface parametrization is consistent with models given by other studies that used the same data but different methods, most notably the standard tomographic approach that inverts for velocity rather than interface structure.

Key words: central Australia, crustal structure, inversion, ray tracing, traveltime.

1 INTRODUCTION

Changes in seismic velocity within the Earth are characterized by both continuous and discontinuous behaviour. In the crust, distinct geological features such as interfaces between layers, fault surfaces, unconformities and the boundaries of intrusive bodies can all cause seismic wave speed to change discontinuously, while gradual changes in density or composition within a layer or body cause seismic velocity to vary smoothly. Seismic traveltime tomography attempts to reconstruct subsurface velocity distribution from the delays between source events and receiver arrivals. To date, most methods of refraction traveltime tomography assume a continuous velocity distribution (e.g. Aki, Christoffersson & Husebye 1977; Evans 1982; Walck & Clayton 1987; Humphreys & Clayton 1990; Benz, Zandt & Oppenheimer 1992; Hole 1992; Achauer 1994; Sato, Kosuga & Tanaka 1996), represented by either constant-velocity blocks or velocity nodes joined by an interpolation function. The disadvantage with this approach is that discontinuous changes in velocity cannot be accurately reconstructed. For example, a test by Wang & Braile (1996) using this type of velocity inversion on synthetic data showed that, while an approximate velocity distribution was recovered, features such as layer interfaces, faults and a pinchout were not resolved. This is not to say that inverting for velocity necessarily results in the total loss of discontinuous features. McQueen & Lambeck (1996) inverted real data for slowness structure in central Australia and were able, by identifying surfaces across which the velocity changed rapidly with distance, to infer the existence of fault structures that correlated well with the results of previous seismic studies and geological surface mapping.

The alternative approach of inverting for interface structure has been applied to both controlled source refraction (White 1989; Hole, Clowes & Ellis 1992) and reflection (Lutter & Nowack 1990) data. Model and observed traveltimes are matched by manipulating the interface geometry with the velocity distribution between interfaces remaining fixed. One obvious disadvantage with this approach is that, if the velocity field between each boundary is not known reasonably accurately *a priori*, artefacts will be superimposed onto the true interface structure. However, if the velocity is known, then the interface inversion will better represent the actual seismic structure.

The ideal approach to seismic tomography is to invert for both interface structure and velocity at the same time. Such inversions have used reflection data (Bishop *et al.* 1985; Chiu,

Kanasewich & Phadke 1986; Williamson 1990; Blundell 1993; Kosloff *et al.* 1996), wide-angle refraction and reflection data (Zelt & Smith 1992; Zelt *et al.* 1996) and a combination of regional earthquake and controlled source data (Sambridge 1990). A problem that all these methods face is how to deal with the possible existence of a large number of different solutions resulting from the trade-off between velocity and interface position. The trade-off is maximized when the traveltime variation can be modelled equally well by velocity or interface perturbations (Blundell 1993). Wang & Braile (1996) found that simultaneously inverting reflection and refraction data helps significantly in minimizing the non-uniqueness of the inversion results.

This paper presents a method of teleseismic traveltime inversion for the determination of interface structure within the crust and mantle lithosphere. The mean (i.e. horizontally averaged) vertical structure of the region being imaged is assumed known (e.g. from surface wave or refraction studies) in the inversion because teleseismic rays do not constrain that part of the velocity structure as well as turning rays. Hence, the trade-off between interface depth and velocity becomes more significant.

The model parametrization used in this paper is designed for a 2-D stratified velocity structure consisting of homogeneous and isotropic layers of variable thickness. The interface between two layers is described by a set of nodes interpolated by cubic splines, with the vertical coordinates of the nodes constituting the unknown parameters that are to be determined by the inversion. The forward problem of determining traveltimes between a wave front located below the crust and a set of receivers on the Earth's surface is solved by an accurate, efficient and robust shooting method. A conjugate gradient method based on the Polak–Ribiere conjugate gradient algorithm (Press *et al.* 1992) is used to solve the inverse problem. The solution requires the minimization of a least-squares-type objective function based on the difference between model and observed traveltimes weighted by a data covariance matrix. The speed of the ray-tracing routine enables the gradient of the objective function to be determined by a simple finite-difference technique, which is favoured over standard analytic formulations due to its superior accuracy in the presence of interfaces with significant curvature.

Once the method is described, we present the results of tests with synthetic data for a multiple interface model. The precision of the reconstruction in the presence of accurate data and *a priori* information on the mean vertical structure is demonstrated, and robustness with respect to noise and inaccurate vertical structure is also investigated. Finally, we illustrate an application of the method to a previously published data set consisting of traveltime anomalies recorded by an in-line array of seismometers across the northern margin of the Musgrave Block, central Australia (McQueen & Lambeck 1996). We compare the solution obtained using an interface parametrization with that of McQueen & Lambeck (1996), who inverted the same traveltime anomalies to obtain a solution parametrized with constant-velocity blocks. We aim to show that the subsurface structural information contained in the teleseismic traveltime residuals can be revealed by inversion for interface geometry, and that interface parametrization represents a valid alternative to velocity parametrization, neither method being complete, but each having advantages for specific data sets.

2 METHODOLOGY

2.1 Model parametrization

The parametrization employed here is for a 2-D stratified velocity structure with constant-velocity layering. The interface between adjacent layers is described by a set of splined node points whose vertical coordinates constitute the unknown parameters that are to be solved. Like White (1989) and Lutter & Nowack (1990), we use cubic spline functions to represent the interface between node points.

The smoothly varying nature of cubic splines means that virtually any smooth interface can be represented. Features such as faults or chevron folds, however, can only be approximated by this parametrization. In addition, each interface is assumed to be single-valued in the independent variable x (the horizontal coordinate), so that intrusive bodies and recumbent folds are again only approximated.

2.2 Solving the forward problem

Given a model structure, the forward problem is to determine the ray paths and traveltimes from a wave front initially located beneath the structure to a set of receivers located on the surface. The forward routine will be used many times by the inversion procedure, so a method that is both quick and reliable is required, and to this end the shooting approach to ray tracing is used. This is preferable to the bending approach, which becomes complex and difficult to handle when the velocity field contains discontinuities (Sambridge & Kennett 1990). The method given here is described in two parts: (1) tracing a ray through one or more interfaces and (2) finding the rays that hit the receivers.

2.2.1 Ray tracing

Since the velocity in each layer is assumed constant, the tracing of a ray from the wave front below the structure to the surface only requires the point of intersection of the ray with each interface and its new gradient upon refraction to be determined. The equation describing a ray is piecewise linear, while the equation describing a segment of the interface is cubic, so the point of intersection of a ray with an interface is given by the solution of a cubic equation. We solve this equation using the Newton–Raphson method with the required initial guess given by the x-coordinate of the point at which the ray intersects a linear segment joining the appropriate pair of interface nodes.

Once the intersection point has been established, the amount of refraction the ray experiences on passing through the interface is calculated by using Snell's law as follows. Let γ_k denote the gradient of a ray in the kth layer ($k = 1, 2, \ldots, r$), where the first layer ($k = 1$) is the bottom layer that contains the incident wave front. Also, let β_k denote the gradient of the interface below the kth layer at the point of intersection with the ray (see Fig. 1). Then the gradient of the ray in the $(k+1)$th layer can be written as

$$\gamma_{k+1} = \frac{\beta_{k+1} \pm \sqrt{(1+\psi_k^2)(v_k/v_{k+1})^2 - 1}}{1 \mp \beta_{k+1}\sqrt{(1+\psi_k^2)(v_k/v_{k+1})^2 - 1}} \qquad k = 1, 2, \ldots, r-1, \tag{1}$$

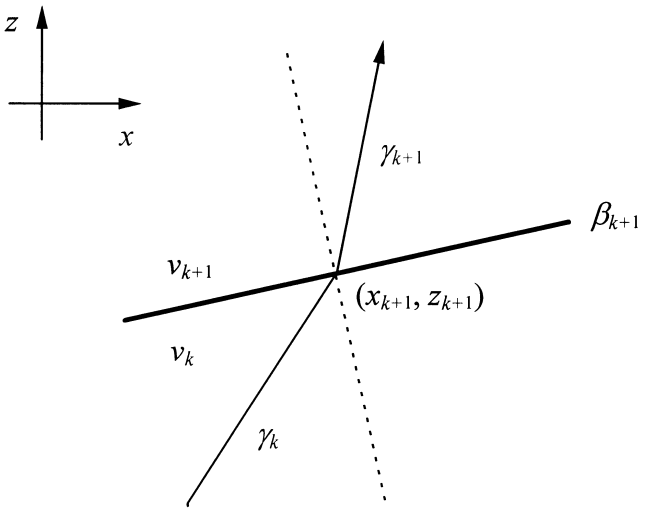

Figure 1. Refraction of a ray at an interface. β_{k+1} is the gradient of the line tangent to the interface at (x_{k+1}, z_{k+1}) while γ_k and γ_{k+1} are the gradients of a ray in the kth and $(k+1)$th layer with velocities of v_k and v_{k+1} respectively.

where v_k is the velocity in the kth layer and $\psi_k = (\gamma_k - \beta_{k+1})/(1 + \gamma_k \beta_{k+1})$. The plus sign in the numerator and the minus sign in the denominator are used when $\psi_k > 0$, and the minus sign in the numerator and the plus sign in the denominator are used when $\psi_k < 0$. The case $\psi_k = 0$ is of no interest because it implies that $\gamma_k = \beta_{k+1}$—the ray and interface are parallel at the 'intersection point'. There are three other interesting features associated with eq. (1). First, if $\gamma_k \beta_{k+1} = -1$, the ray and interface are perpendicular, and the ray is transmitted with no change in gradient: $\gamma_{k+1} = \gamma_k$. Second, if the expression under the square root sign is negative, then the above expression for γ_{k+1} is indeterminate. This case corresponds to total internal reflection; note that it can only occur if $v_k < v_{k+1}$. Lastly, if the denominator of eq. (1) is zero, the refracted ray is vertical.

Fig. 2 shows an example of shooting a spread of 204 equally spaced rays from an incident planar wave front of gradient -0.3 using the above method. We assume that a plane-wave approximation of the incident wave front is generally acceptable for teleseismic sources. The seven-layer structure is described by six interfaces, each consisting of 17 evenly spaced splined node points. Velocity increases with depth, with the exception of the third layer below the surface, which is a low-velocity layer. Rays that pass upwards from a higher-velocity layer to a lower-velocity layer are focused by concave-up portions of the interface and defocused by concave-down portions. The opposite is true for rays passing upwards from the low-velocity layer.

2.2.2 *Obtaining the required rays*

The previous section describes how to trace rays through a medium with an arbitrary number of layers, but the forward problem is solved only when a first-arrival ray path to each station has been found and the corresponding traveltime calculated. An initial shoot, such as that shown in Fig. 2, provides information about the behaviour of ray paths in the vicinity of the ray path being sought. This information can be used to identify the ray that hits a particular station. An approximation to the true ray can be obtained by linearly interpolating between two rays from the initial shoot that bracket the station being targeted, but this method is not precise when interfaces with significant curvature are present. We formulate a scheme that uses the linear interpolation method to find an initial guess ray for each station before applying an iterative correction strategy that accurately and efficiently finds the required rays.

Let δs denote the distance between the target station and the initial guess ray at the same z coordinate as the target station, and let δw be the distance between the origin of the initial guess ray on the wave front and the origin of the ray that does intersect the station (see Fig. 3). If γ_k is the gradient of the initial ray in the kth layer and β_k is the gradient of the interface below the kth layer where it is intersected by the ray (as in eq. 1), then δs and δw are approximately related by

$$\delta w \approx \kappa \delta s \prod_{k=1}^{r} \sqrt{\frac{[(1+\beta_k\gamma_k)/(\gamma_k - \beta_k)]^2 + 1}{[(1+\beta_{k+1}\gamma_k)/(\gamma_k - \beta_{k+1})]^2 + 1}}. \quad (2)$$

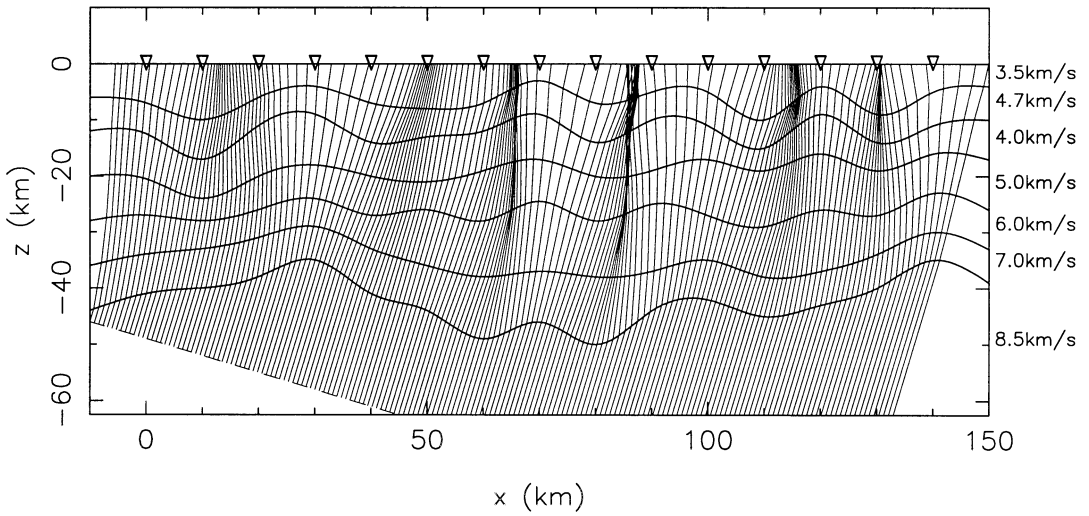

Figure 2. An even spread of 204 rays shot from an incident planar wave front with gradient -0.3 through a seven-layer structure. The symbol ▽ represents a station located on the surface, while thick solid lines denote interfaces and thin solid lines denote ray paths. The incident wave front is represented by the dashed line.

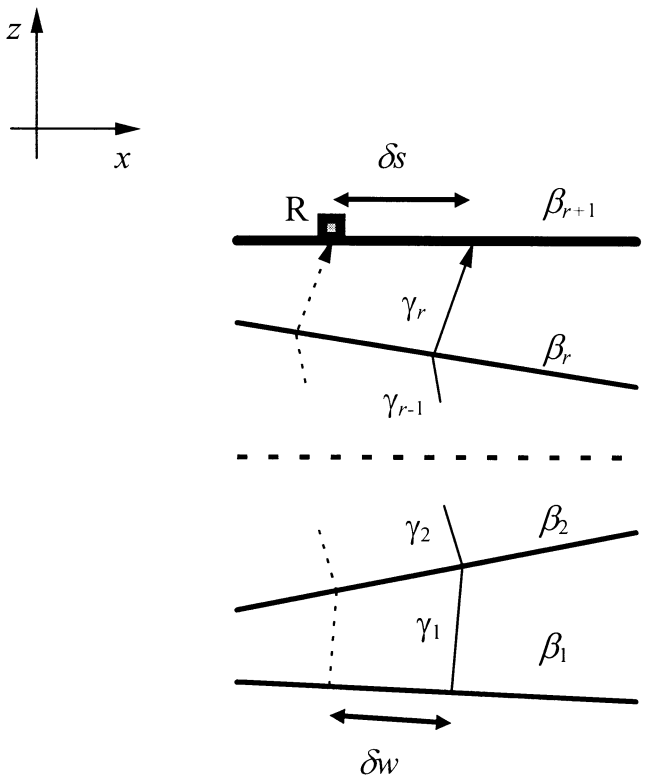

Figure 3. Parameters used in eq. (2). R is the receiver, δs is the distance on the surface between the initial ray and the receiver, δw is the distance on the incident wave front between the initial ray and the required ray, and r is the number of layers. The interfaces in this figure are linear, but they need not be for eq. (2) to work.

Note that β_1 is the gradient of the wave front at the point of projection of the ray, while $\beta_{r+1}=0$ is the gradient of a horizontal line passing through the receiver. In eq. (2), κ is a correction factor for the ray. If κ is set to 1, then eq. (2) represents an exact relationship between δw and δs for linear interfaces. The correction factor κ can be seen as a measure of the effective curvature of all the interfaces inside the region bracketed by the two original rays and is calculated as follows. For two rays a and b that bracket a given station, let d_1 be their distance of separation at the same z-coordinate as the station. In eq. (2), let $\kappa=1$ and solve for δs, where δw is the distance between the two bracketing rays on the wave front, and γ_k and β_k are the ray and interface gradients associated with ray a. Then $d_2=\delta s$ would be the distance between the two bracketing rays at the surface in the absence of interface curvature and $\kappa=d_2/d_1$. Hence, once κ has been calculated from the initial shoot for a particular ray, eq. (2) can be used iteratively and will converge rapidly to the correct two-point ray.

Tests with various structures showed that the implementation of the iterative correction scheme involving eq. (2) is more desirable than using only linear interpolation with a large number of rays in the initial shoot. Typically, we found that the first iteration of the method reduced the average traveltime error of the linear interpolation by more than a factor of 10. To achieve comparable accuracy with linear interpolation requires the projection of approximately three times the number of rays in the initial shoot. Since a single iteration of eq. (2) involves the reshooting of only the same number of rays as there are stations, it is clearly a much more economical approach. In addition, the iterative scheme is more amenable to an accuracy criterion, because if any ray does not hit the surface within a specified tolerance, it can simply be reshot with a significant increase in accuracy.

Fig. 4 shows the first-arrival rays to each station from two incident wave fronts with gradients ± 0.3 through the same structure shown in Fig. 2. Each ray hits the surface within 5 mm of the target station and none of the rays requires more than four iterations of eq. (2) to achieve this accuracy. Note the effect that interface geometry has on ray coverage, with the first-arrival ray paths tending to avoid the laterally slow regions. Traveltimes are calculated by integrating slowness (inverse of velocity) along each ray path. Where more than one ray (from the same wave front) reaches a receiver, the ray with the minimum traveltime is selected.

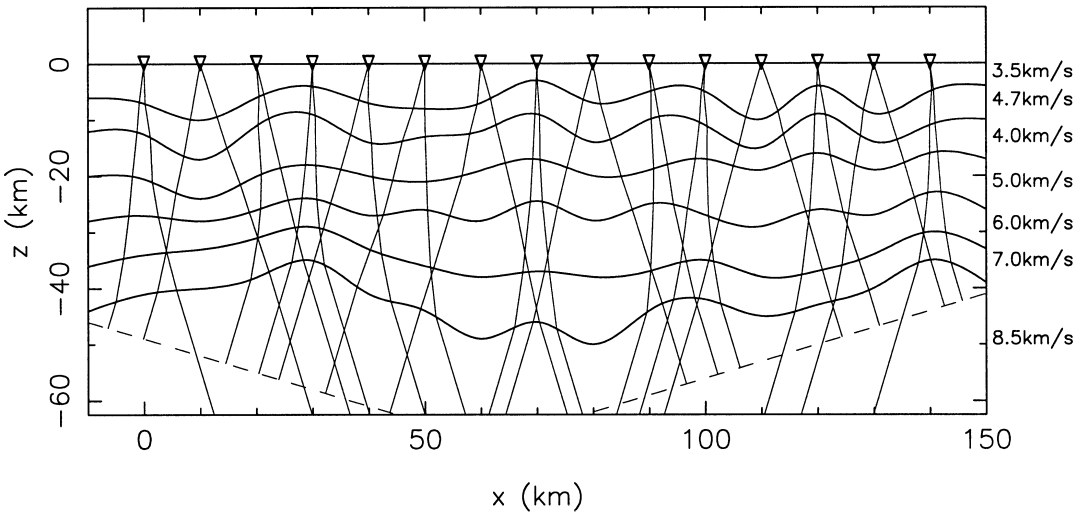

Figure 4. First-arrival rays to each station from two incident wave fronts impinging on the structure shown in Fig. 2. The wave fronts have gradients of -0.3 (the initial shoot for this wave is shown in Fig. 2) and $+0.3$.

2.3 Solving the inverse problem

The inverse problem is to use the observed data in conjunction with the model predictions to reconstruct the interface geometry of a region subject to the assumptions inherent in our parametrization. This can be treated as an optimization problem, where a function of many independent variables is defined, with the object being to determine the values of these variables such that the function assumes a sufficiently small value.

2.3.1 *Choice of the objective function*

The function to be minimized, referred to as the objective function, is a measure of how well the predictions of the model agree with the observed data:

$$S(\mathbf{m}) = [\mathbf{d}_{\rm mod}(\mathbf{m}) - \mathbf{d}_{\rm obs}]^{\rm T}\mathbf{C}_{\rm D}^{-1}[\mathbf{d}_{\rm mod}(\mathbf{m}) - \mathbf{d}_{\rm obs}], \tag{3}$$

where $\mathbf{d}_{\rm mod}$ is the vector of traveltimes for the model and $\mathbf{d}_{\rm obs}$ is the vector of observed traveltimes. The dimension of these vectors is N, corresponding to the number of receiver stations multiplied by the number of distinct wave fronts for each set of traveltimes. The vector $\mathbf{m}$ is the set of depths to one or more interfaces, and has a dimension M, equal to the number of node points. The Euclidian or L_2 norm is used here, with the data covariance matrix $\mathbf{C}_{\rm D}$ introduced to account for error estimates in the case of real data. Of course, other terms may be added to eq. (3) to help constrain the final model; for example, Tarantola (1987) also includes a term that attracts the solution to regions of model space near an *a priori* model. Although it does not appear explicitly in our objective function, the *a priori* or initial model estimate does assume a significant role in our model reconstruction. In Section 3, we show that teleseismic traveltime residuals, adjusted for source-time uncertainty by having their mean removed, do not constrain average vertical structure. Consequently, the average vertical structure of the inverted model is effectively determined by the initial model estimate.

2.3.2 *Conjugate gradient method*

Hestenes & Stiefel (1952) first suggested the idea of conjugate gradient methods in regard to solving linear equations. Fletcher & Reeves (1964) subsequently applied it to unconstrained optimization. Conjugate gradient methods find a minimum by using information from the quadratic form of the objective function. For $S(\mathbf{m}_0)$ at some point $\mathbf{m}_0$ in model space, the objective function at a new point $\mathbf{m} = \mathbf{m}_0 + \delta\mathbf{m}$ can be approximated by the Taylor series expansion

$$S(\mathbf{m}) \approx S(\mathbf{m}_0) + \nabla_{\mathbf{m}} S(\mathbf{m}_0)\,\delta\mathbf{m} + \frac{1}{2}\delta\mathbf{m}^{\rm T}\mathbf{H}\,\delta\mathbf{m}, \tag{4}$$

where $\mathbf{H}$ is the matrix of second-order partial derivatives of S at $\mathbf{m}_0$, called the Hessian matrix. Objective functions that satisfy eq. (4) exactly are quadratic, and are best suited to minimization by the conjugate gradient method, though non-quadratic objective functions may also be minimized by this technique. The conjugate gradient method that we employ is based on the general Polak–Ribiere conjugate gradient code contained in Press *et al.* (1992) and will not be described again here. We will, however, describe the process used to calculate the gradient vector $\nabla_{\mathbf{m}} S(\mathbf{m})$ (containing M components $\partial S(\mathbf{m})/\partial m_i$, $i = 1, 2, \ldots, M$) that is required by the method.

Two separate techniques were considered for the calculation of $\nabla_{\mathbf{m}} S(\mathbf{m})$. In the finite-difference formulation, we perturb each m_i by an amount Δm_i and re-evaluate the objective function to get $S(\mathbf{m})_{\Delta m_i}$. Then the forward difference approximation is

$$\frac{\partial S(\mathbf{m})}{\partial m_i} \approx \frac{S(\mathbf{m})_{\Delta m_i} - S(\mathbf{m})}{\Delta m_i}. \tag{5}$$

We can justifiably use a very small value for Δm_i (typically 3–5 m) because of the high precision of the ray-tracing routine. An alternative approach to calculating $\nabla_{\mathbf{m}} S(\mathbf{m})$ is to use an analytic approximation. By the chain rule

$$\frac{\partial S(\mathbf{m})}{\partial m_i} = \frac{\partial S(\mathbf{m})}{\partial t_j(\mathbf{m})}\frac{\partial t_j(\mathbf{m})}{\partial m_i}, \tag{6}$$

where $t_j (j = 1, 2, \ldots, N)$ is the jth component of $\mathbf{d}_{\rm mod}$, the vector of model traveltimes. Provided we can compute the complete $M \times N$ matrix of Fréchet derivatives $\partial t_j(\mathbf{m})/\partial m_i$, then $\nabla_{\mathbf{m}} S(\mathbf{m})$ is easily obtained from eq. (6). Nowack & Lyslo (1989) give an analytic expression for these derivatives that is accurate to first order. Using the notation of Section 2.2, their expression reformulated in terms of ray and interface gradients is

$$\frac{\partial t}{\partial m} = \left[\frac{1}{v_k}\sqrt{\frac{(\gamma_k - \beta_k)^2}{1+\gamma_k^2}} - \frac{1}{v_{k-1}}\sqrt{\frac{(\gamma_{k-1} - \beta_k)^2}{1+\gamma_{k-1}^2}}\right]\left(\frac{1}{1+\beta_k^2}\right)\frac{\partial z_{\rm int}}{\partial m}, \tag{7}$$

where the i and j subscripts have been dropped for simplicity and the node resides in the kth interface. In eq. (7), $z_{\rm int}$ is the point at which the ray intersects the interface, so $\partial z_{\rm int}/\partial m$ describes the rate of change of this point with respect to the model parameter m, and may be calculated by perturbing m and measuring the corresponding change in $z_{\rm int}$.

Synthetic tests with various models demonstrated that the analytic method was computationally rapid and reasonably robust for single interfaces or multiple interfaces with modest interface curvature. However, when more than one interface with significant curvature was present (a situation encountered in our synthetic and real data examples in Sections 3 and 4), the method based on Nowack & Lyslo's first-order approximation produced relatively small reductions in the objective function per iteration and poor model reconstructions. In contrast, the finite-difference formulation of $\nabla_{\mathbf{m}} S(\mathbf{m})$ converged faster and produced model reconstructions that were much closer to the synthetic test model. A probable explanation for this difference is that the expression for the partial derivative given by Nowack & Lyslo (1989) does not adequately account for interface and wave-front curvature while the finite-difference approximation does. In light of its superior accuracy in the presence of significant interface curvature, we employ the finite-difference approximation of $\nabla_{\mathbf{m}} S(\mathbf{m})$ in all the inversions presented in this paper, and since the forward calculation (Section 2.2) is so fast, the computational inelegance of this approach is not encumbering.

3 RESULTS

3.1 test with synthetic data

We first test how accurately the interface inversion algorithm can solve for a known structure. A set of rays is traced through a given model to get traveltimes (the synthetic data) and these

times are then used in conjunction with a starting model to reconstruct the original interface geometry. Tests using synthetic data can also provide valuable insight into how sensitive the method is to data noise and inaccurate knowledge of the mean (i.e. horizontally averaged) vertical structure.

The model chosen for the synthetic tests consists of a three-layer structure as shown in Fig. 5(d). Each of the two interfaces is parametrized by 18 equally spaced node points and the velocity discontinuity across each interface is 1.5 km s^{-1}. Although not obvious in Fig. 5(d), a surface topography that does not exceed 1 km in height or depth is also included in the model. Synthetic data are generated by ray tracing from the three incident wave fronts to the receivers on the surface. Receiver separation varies between 8 and 10 km across the 130 km line, which contains 16 stations. The traveltimes are plotted in Figs 5(a)–(c) and correspond to the waves with gradients of 0.5, 0.0 and -0.5 respectively. These times have been reduced to highlight the variations in traveltime caused by changes in lateral structure. The reduced traveltimes are defined by $t' = t - d/v_x$, where t is the actual traveltime of the ray from the wave front to the surface, d is the horizontal distance from a reference station and v_x is the horizontal component of velocity of the wave in the bottom layer. For the waves with gradient 0.5 and -0.5, the reference stations are at $x = 130$ and 0 km respectively; the wave with gradient 0.0 has $t' = t$ for all rays.

The starting model for the inversion is a 1-D structure (except for the surface topography) consistent with what could be determined from a refraction and wide-angle reflection survey of the region. In this first test, the horizontal positions of the nodes along each interface and the velocity of each layer are the same as those used in the model from which the synthetic data are obtained, and the depth to each interface in the starting model is equal to the average depth of the corresponding interface in the test model.

The results of the inversion are shown in Figs 6(a)–(c). After 40 iterations, the objective function (Fig. 6a) has dropped to less than 0.0001 per cent of its original value, at which point the rms data residual (the rms difference between observed and model traveltimes) is less than 0.063 ms. To track the behaviour of the model throughout the inversion process, a model misfit function $E(\mathbf{m})$ has been calculated at each iteration; this misfit function is defined to be the rms distance between corresponding node points in the test model and the reconstructed model:

$$E(\mathbf{m}) = \left[\frac{(\mathbf{m}_{\text{true}} - \mathbf{m})^{\text{T}} (\mathbf{m}_{\text{true}} - \mathbf{m})}{M} \right]^{1/2}, \tag{8}$$

where the M-dimensional vectors $\mathbf{m}_{\text{true}}$ and $\mathbf{m}$ are the set of interface depth parameters of the test model and the reconstructed model respectively. In this example, the model misfit function (Fig. 6b) shows that the most significant reductions occur over the first few iterations, and in fact the algorithm produces only trivial improvements after about 8–10 iterations. The initial misfit is approximately 3 km while the final misfit is around 0.3 km. A comparison between the reconstructed model and the test model (Fig. 6c) shows that the structure is recovered almost exactly. Only at the endpoints, where the boundary nodes are not well constrained by the rays (see Fig. 5d), are the two models perceptibly different. The lack of information about these regions in the data explains why the model misfit function is not much closer to zero at the final iteration. The monotonic behaviour of the model misfit function illustrates the stability and robustness of the inversion algorithm.

The above test shows that, given accurate data and *a priori* information on the mean vertical structure, the interface inversion algorithm is capable of producing accurate results. Before applying the method to real data, however, a number of other synthetic tests should be carried out. First, the problem of event-time uncertainties needs to be addressed since earthquakes are uncontrolled events. A common way of dealing with event-time uncertainty (e.g. Humphreys & Clayton 1990) is to remove the mean from each residual set (each event producing a set of residuals) under the assumption that the mean vertical structure of the initial model is correct. Setting the mean residual to zero means that the iterative inversion process will only result in lateral changes to the initial model. In all the following examples, the mean has been removed from the traveltime residuals.

An intrinsic property of real data is that they contain noise, and hence the robustness of the inversion with respect to noisy data needs to be tested. In the next example, we add Gaussian (normally distributed) noise to the synthetic traveltime data set of Figs 5(a)–(c). This is done by choosing a standard deviation for each source–receiver pair and generating Gaussian noise so that the error added to each traveltime is related to the corresponding standard deviation according to a normal distribution. The standard deviations $\{\sigma_j\}$, $j = 1, 2, \ldots, N$, employed in this example vary between 0.02 and 0.08 s. When inverting the noise data, these strandard deviations are used in the data covariance matrix (whose ijth component is $[C_{\text{D}}]_{ij} = \delta_{ij}\sigma_j^2$) that forms part of the objective function (see eq. 3). Fig. 7 shows the results of this inversion, which uses the same starting model as the Fig. 6 example. One obvious feature of the model misfit function (Fig. 7b) is that, after an initial period of decrease, it gradually begins to increase again from about iteration 7. Beyond this point, the algorithm is generating structure that is consistent with the noise but is not part of the true model. Correspondingly, the objective function continues to decrease monotonically, albeit slowly, throughout the remaining inversion process. Evidently, the best model occurs at iteration 7, but in the absence of a model misfit function, some other criterion is required to indicate when the best model has been achieved. One possibility is to stop the iterative procedure once the objective function is composed of residuals of a similar magnitude to the standard deviations of the data noise. An alternative is to base the cut-off point on the shape of the objective function versus iteration curve. A feature of Fig. 7(a) is that the curve flattens out after the optimum model has been achieved. Tests involving a number of different synthetic models indicate that the best place to cease the iterative process occurs when the objective function has a value approximately 33 per cent greater than its plateau value. This criterion and the one based on the rms traveltime residuals provide a rough location of the model misfit minimum, but further investigation of methods aimed at a more accurate location of the minimum is not warranted since the model misfit function increases only gradually once the optimum model is achieved. Figs 7(c) and (d) show the reconstructed model after 7 and 25 iterations respectively. Both models recover the basic structure of the test model. The main reason why the model at iteration 25 is a poorer fit is because of its

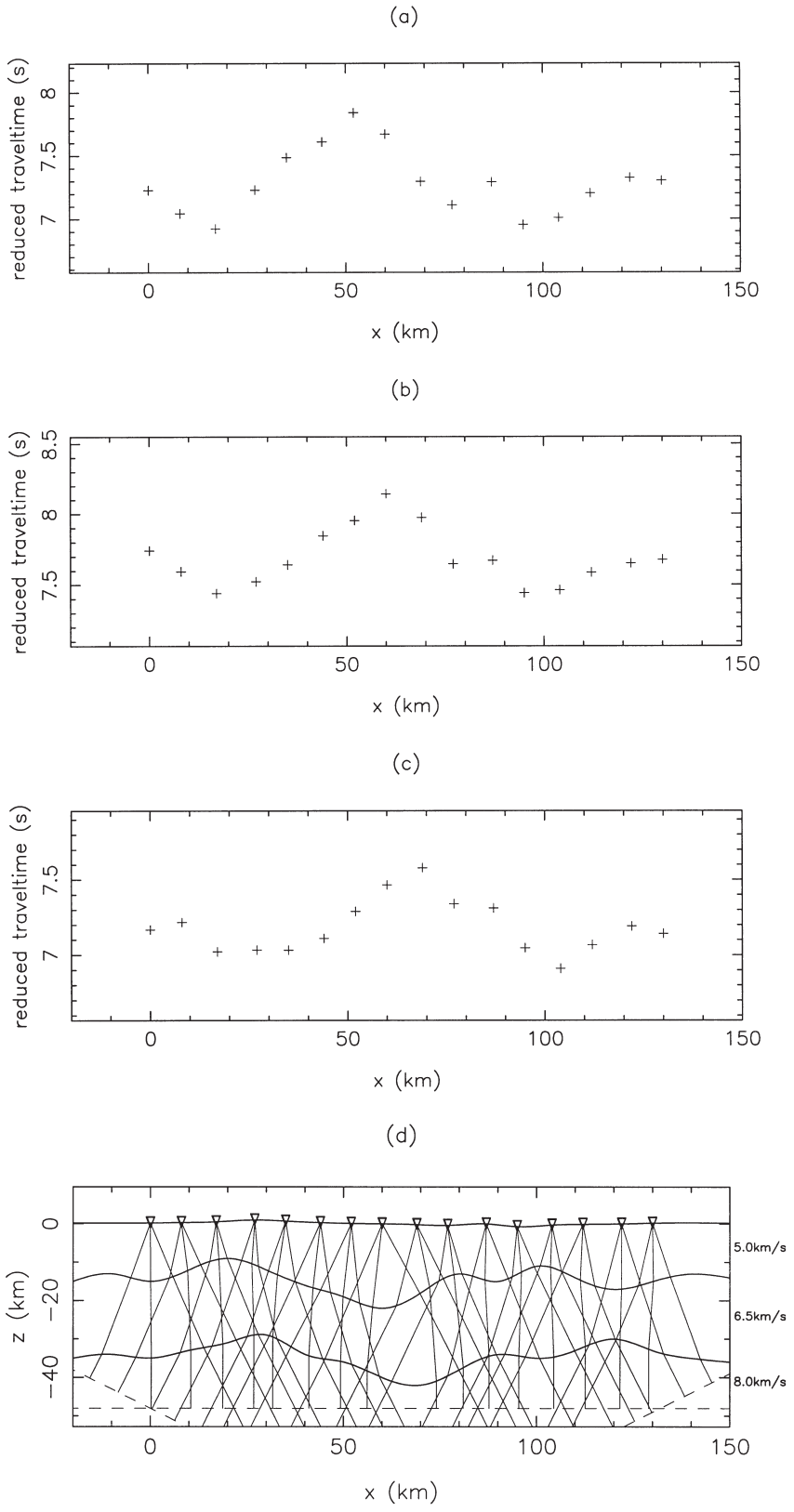

Figure 5. Model and data chosen for the synthetic tests. The reduced traveltimes for the waves with gradients 0.5, 0.0 and −0.5 are shown in (a), (b) and (c) respectively. The three-layer model is shown in (d) along with the incident wave fronts (dashed lines) and ray paths (thin solid lines). The surface topography does not significantly affect the appearance of the reduced traveltime plots.

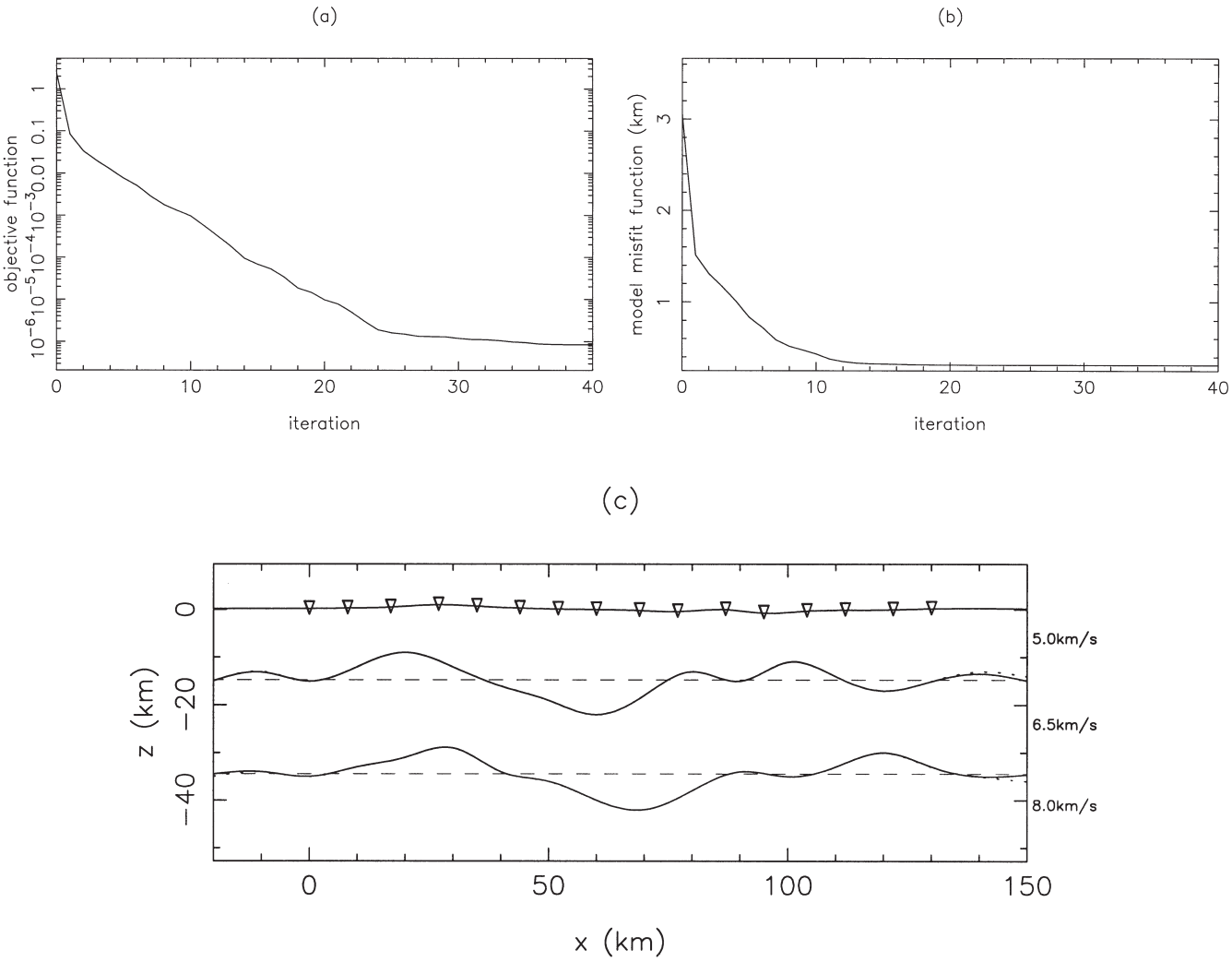

Figure 6. Ideal case inversion results. (a) Objective function versus iteration number, (b) model misfit function versus iteration number, and (c) comparison of final model interface structure (solid lines) with synthetic model interface structure (dotted lines). The starting model for the inversion is shown by the dashed lines.

behaviour near the endpoints of the interfaces, where ray coverage is sparse.

Apart from data noise, other factors that will contribute to the error in the final model include (i) choosing interface depths in the initial model that are not near the mean depth of the corresponding true interface and (ii) choosing incorrect layer velocities. These two factors represent different aspects of uncertainty in defining the mean vertical structure. Fig. 8(a) demonstrates the result of inverting when the two horizontal interfaces in the starting model are each in error by 4 km (−4 km for the top interface and +4 km for the bottom interface). While the correct mean vertical positions of the interfaces have not been recovered by the inversion, their lateral structure is accurately represented. An interesting question that poses itself here is whether the method will reproduce the true model in this situation if no event-time errors were present and the traveltime residuals were absolute. The answer is no, because a vertical shift of one interface can be traded off against the vertical shift of another. The solution of this inverse problem is not unique with respect to average vertical structure because of the near-vertical incidence of the ray paths.

Fig. 8(b) demonstrates the effect of inverting when the velocities in the top two layers are 0.2 km s^{-1} too slow and the velocity in the bottom layer is 0.1 km s^{-1} too slow. The correct interface geometry is approximately recovered after seven iterations. If no source-time errors are present in the data and absolute traveltime residuals are inverted, then the result is similar to Fig. 8(b) but with a positive vertical shift of each interface, which compensates for the errors in layer velocity.

The examples shown in Fig. 8 illustrate several things. First, this type of data does not accurately constrain mean vertical structure; the mean vertical structure in the solution is simply inherited from the starting model used in the inversion. Second, in order for the interface inversion method to recover lateral structure, an accurate mean vertical structure is not necessary. Finally, accounting for event-time errors by mean residual removal does not result in the loss of important information from the reconstructed model.

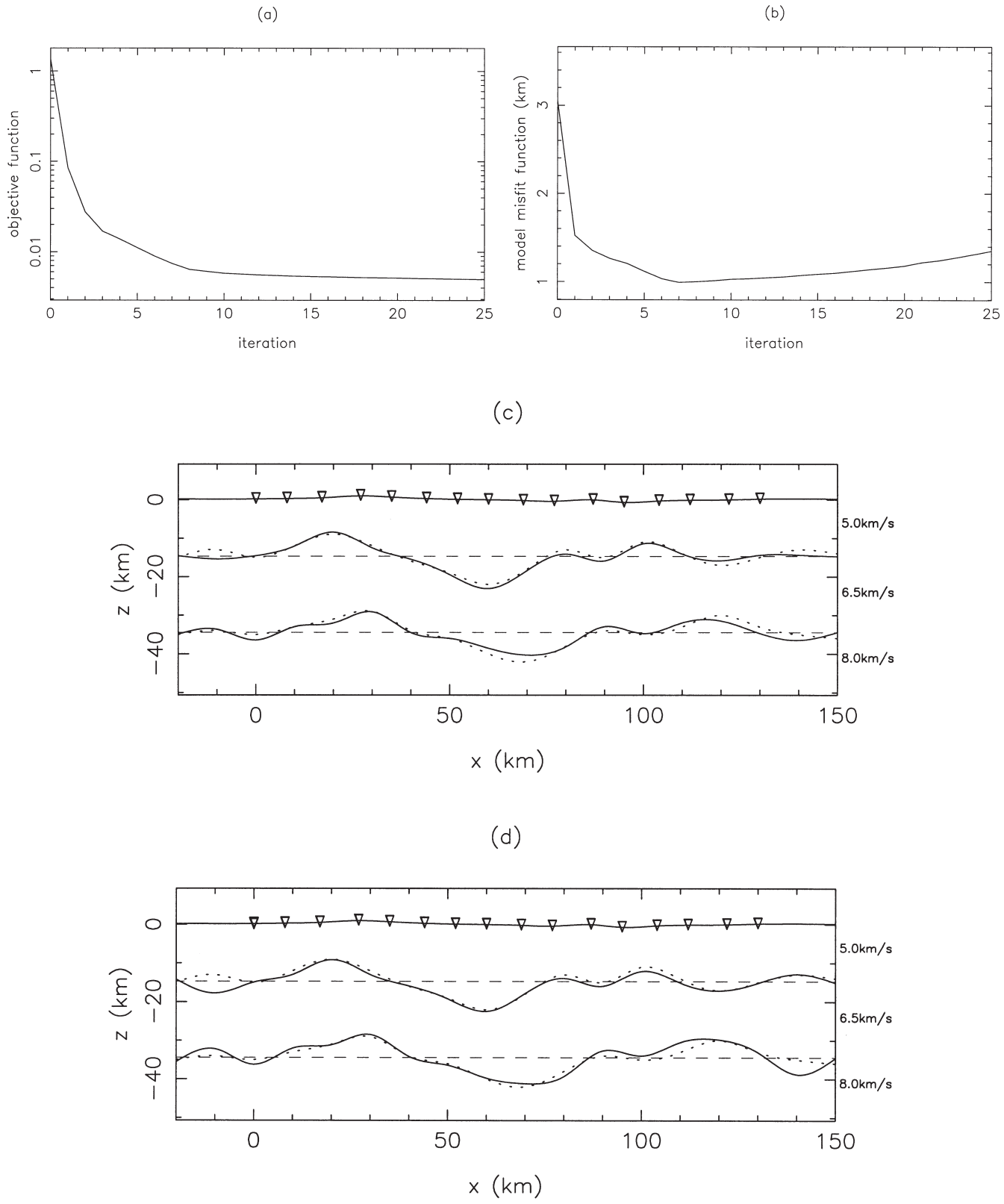

Figure 7. Inversion results for noisy data. (a) Objective function versus iteration number, (b) model misfit function versus iteration number, (c) comparison of final model (at iteration 7) interface structure (solid lines) with synthetic model interface structure (dotted lines), and (d) comparison of final model (at iteration 25) interface structure (solid lines) with synthetic model interface structure (dotted lines). In both (c) and (d), the starting model is indicated by the dashed lines.

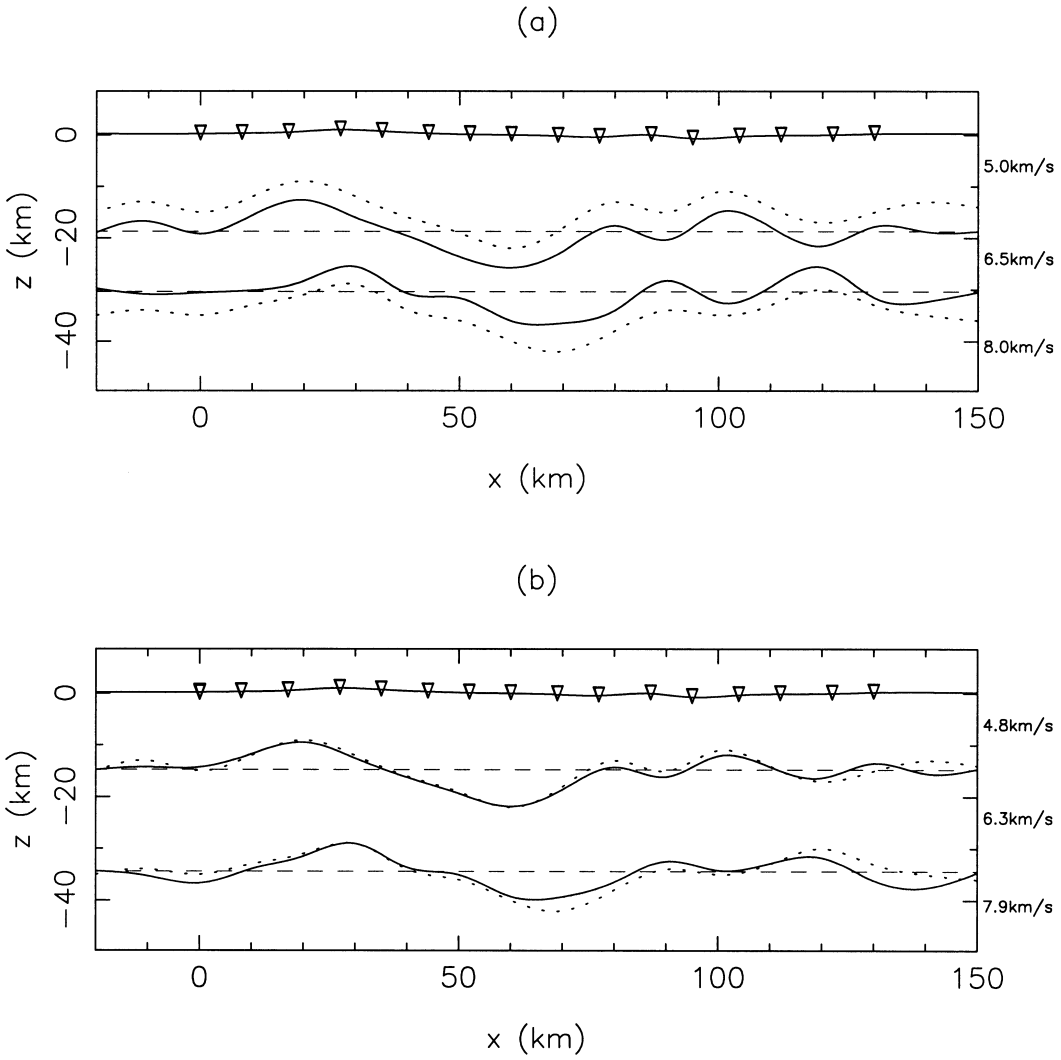

Figure 8. Inversion results with poor velocity or initial depth estimation. Final model interfaces are denoted by solid lines, synthetic model interfaces are denoted by dotted lines, and starting models are denoted by dashed lines. (a) Final model (at iteration 10) with poor initial depth estimation, and (b) final model (at iteration 7) with inaccurate velocity estimation.

The horizontal node separation we choose for our reconstructed model plays an important role in regularizing the inverse problem because it controls the minimum allowable wavelength of the interface features. The results of several synthetic tests indicate that the optimum node separation in the presence of a good angular coverage of rays (such as Fig. 5d) is approximately equal to the station separation; smaller node separations tend to lead to the generation of spurious structure.

Once a solution model has been obtained by an inversion procedure, it is common practice to analyse the quality of the solution by quantitative means. The formulation of resolution and *a posteriori* covariance matrices are popular ways of doing this (e.g. Lutter & Nowack 1990; Zelt & Smith 1992; McCaughey & Singh 1997) because they describe how well each parameter is independently resolved by the data, and give the uncertainty in the value of each parameter. One drawback is that they are derived from linear theory, so their role in analysing the solutions of non-linear problems is limited. In particular, the error estimates given by the *a posteriori* covariance matrix should be viewed in a relative rather than absolute sense (Zelt & Smith 1992). We calculated the *a posteriori* covariance matrix (as defined by Tarantola 1987) for the example illustrated in Fig. 7(c). The main features of interest are the relatively large uncertainties associated with the nodes at the endpoints of the interfaces, and the uncertainties in the lower interface nodes being on average 33 per cent greater than those in the upper interface. The first phenomenon is caused by the lack of ray coverage in the vicinity of the endpoint nodes, while the second is a consequence of the larger velocity ratio between the upper two layers compared to the lower two layers. The correlation between model parameter uncertainties can be calculated from the elements of the *a posteriori* covariance matrix (Tarantola 1987). A strong correlation indicates that the two parameters have not been independently resolved by the data set. Apart from the endpoint nodes, most parameters in Fig. 7(c) were quite well resolved. Strong anticorrelations occurred between nodes in adjacent interfaces, illustrating the trade-off between interface positions.

3.2 Application to central Australian data

On a crustal scale, the geology of central Australia consists of a number of intracratonic sedimentary basins separated by uplifted blocks of basement (Plumb 1979). From north to south, there is the Arunta Block, which hosts the much smaller Ngalia Basin, the Amadeus Basin, the Musgrave Block and the Officer Basin; the area that these structures occupy is approximately 750 km by 750 km. Geological evidence (Wells *et al.* 1970; Plumb 1979) suggests that the exposed crust varies in age from Proterozoic (for the uplifted basements) to Carboniferous (for the sedimentary basins). A model for the evolution of this region has been proposed by Lambeck (1983), who describes the formation of the structures in terms of horizontal compressive forces acting on an inhomogeneous viscoelastic lithosphere. The deformation caused by compression is increased by erosion of the uplifted areas and sediments being deposited in the downwarps to form the basins. Thrust faulting is predicted to occur as a result of cumulative bending stresses. More recently, Lindsay & Korsch (1991) used sequence stratigraphy to identify three major stages of tectonic development. The first two stages consisted of distinct periods of extension commencing at about 900 and 580 Ma, while the final stage involved a major compressional event beginning at approximately 450 Ma. The compressional event is primarily responsible for the present-day structure of the basin margins.

Teleseismic traveltime residuals from several different surveys have previously been used to constrain the crustal structure of central Australia (Lambeck & Penney 1984; Lambeck, Burgess & Shaw 1988; Lambeck & Burgess 1992; McQueen & Lambeck 1996). To test the interface inversion method presented in Section 2, we use the data of McQueen & Lambeck (1996) from the Musgrave Line. This data set consists of events recorded by 26 stations positioned along a north–south line from Lake Amadeus in the Amadeus Basin to near the southern margin of the Musgrave Block. We compare the results of the interface inversion method with those of the more standard tomographic methods used by McQueen & Lambeck (1996) and the forward modelling of Lambeck & Burgess (1992).

The methods used to pre-process the Musgrave Line data into the form used by McQueen & Lambeck (1996) are described in detail by Lambeck & Penney (1984) and Lambeck *et al.* (1988). We include a brief description here for completeness. Observed traveltimes t_{ij}^0 from each event (j) to each receiver (i) are found by comparing arrival times with the monthy listings of the US Geological Survey, National Earthquake Information Service (NEIS). Theoretical traveltimes t_{ij}^c are determined from the Herrin *et al.* (1968) traveltime model. Hence, a differential traveltime anomaly is defined by

$$\Delta t_{ij} = t_{ij}^0 - t_{ij}^c - \frac{1}{m}\sum_{i=1}^{m}(t_{ij}^0 - t_{ij}^c) \tag{9}$$

for a set of m receivers. The last term in eq. (9) subtracts the mean residual for each event so that the data are insensitive to source-time uncertainties, as outlined in Section 3.1. The next step is to determine an average station anomaly for events that originate in a given source region. For a set of events from each source region, the amomalies are written as

$$\Delta t_{ij} = a_j + t_i + \varepsilon_{ij}, \tag{10}$$

where j ($j = 1, 2, \ldots, n$) now ranges over all the rays from a particular source region. In eq. (10), ε_{ij} is the measurement error, a_j is the event correction and t_i is the station anomaly. The nm equations (10) are solved for the $n + m$ unknowns $\{a_j\}$ and $\{t_i\}$ by a least-squares minimization of the error. From the solution of eq. (10), a set of n error values are produced for each source region–receiver pair. In our inversion, the ith diagonal element of the data covariance matrix is set equal to the variance of the n error values for station i, so that stations whose traveltime anomaly is more precisely defined have a greater effect on the objective function. Table 1 shows the number of events, azimuth range and distance range for each source region.

The receiver array that forms the Musgrave Line traverses about 70 km of the Amadeus Basin and 150 km of the Musgrave Block. Hence, the initial model used in the inversion should recognize characteristics of both the uplifted block and the sedimentary basin. While no deep reflection/refraction model has been published for the Musgrave Block, a deep reflection model (PBW01) for the Amadeus Basin can be found in Collins (1988). This shows an 8.75 km thick layer of sediment overlying middle and lower crustal layers of higher velocity. The initial model (Fig. 9) we chose for the inversion is based on PBW01, but we increased the average crustal velocities by 0.3 km s^{-1} in acknowledgment of the higher velocities that are likely to be present in the Musgrave Block. This change means that the average crustal velocity of our initial model is very similar to that found by Bowman & Kennett (1993) for the western and central Australian crusts using local and regional earthquake traveltimes.

The azimuth of the receiver array is about 5°, but not all source–receiver pairs lie in this plane. Using out-of-plane sources in a problem treated strictly in two dimensions could result in artefacts appearing in the final model. Three source regions, Japan, South Sandwich Islands and Kuril, all lie within 10° of the receiver array azimuth, so the errors in traveltime anomalies, caused by projecting the incident wave fronts into the plane of the section, are small. These data are used in the inversion without further correction.

A total of 87 nodes are used to parametrize the interfaces of the inversion model, and the horizontal separation distance between adjacent nodes is 10 km in all cases. The data do not justify the use of more interface parameters (note that station separation is about 10 km on average) and the use of fewer nodes will compromise the ability of the method to resolve detailed structure. Fig. 10 shows the data fit and model structure after nine iterations of the inversion procedure, which inverted the data from all three source regions simultaneously.

Table 1. Parameters associated with the source regions.

Source region	Distance range (°)	Azimuth range (°)	No. of events
Japan	53–65	358–12	10
S. Sandwich Is.	92–97	191–194	5
Kuril	69–79	10–17	3
Mindanao	31–37	348–353	4
SE Indian Rise	28–33	211–222	2
New Zealand	40–44	115–119	2
Fiji	43–52	89–98	13
Kermadec	44–46	105–109	3

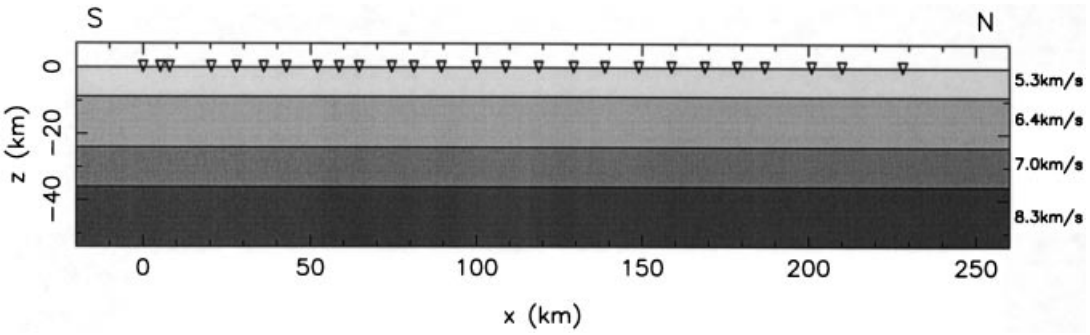

Figure 9. The starting model for the inversion of Musgrave Block data. Velocities in each layer are 0.3 km s^{-1} faster than those given by Collins (1988), based on the Amadeus Basin deep reflection seismic data.

At this point, the objective function has decreased to less than 5 per cent of its original value, corresponding to a rms data misfit reduction of 78 per cent. With further iterations, the objective function versus iteration curve began to achieve a plateau value. Stopping the iterative process after nine iterations is consistent with the convergence criteria described for the test problem in Section 3.1. The improvements in data misfit are illustrated in the plots of the observed and model traveltime anomalies (Figs 10a–c) for each source region. Ray coverage through the final model is shown in Fig. 10(d), and gives an indication of how well individual model parameters are constrained by the data. Fig. 10(e) shows the final model with three interpreted 'fault structures' superimposed. These have been inferred to exist by correlating known (or suspected) fault features on the surface with large slopes common to adjacent interfaces. Our interpretation relies on the understanding that the model parametrization can only provide a smoothed approximation to interface discontinuities such as faults. Hence, the strongly undulating nature of the interfaces between $x = 0$ and 70 km is consistent with the presence of several faults. Note that the deflection of a single interface cannot in itself describe a fault. Only if similar deflections are present in adjacent interfaces can a fault line be drawn and fault-dip estimated. According to this criterion, we might be tempted to place a fault at about $x = 220$ km, but the poor ray coverage in this region of the model would make such an interpretation unreliable.

Interpreted faults 1 and 2 (Fig. 10e) correspond to the Lindsay and Wintiginna Lineaments respectively, which represent major magnetic lineaments (Lambeck & Burgess 1992). From this solution, they both have a northerly dip of about 80°. Interpreted fault 3, with a southerly dip of approximately 70°, corresponds to the Mann Fault, a major thrust fault, which, along with its eastern continuation the Ferdinand Fault, forms a large structure that extends across almost the entire width of the block (Lambeck & Burgess 1992). Without the *a priori* knowledge that faulting is the principal structural feature of the Musgrave Block, geological interpretation of the model would be difficult. Even so, there is still some uncertainty in the positioning of fault surfaces and the estimated dip angles. For example, interpreted fault 3 could be horizontally translated some ± 10 km or varied in dip by about $\pm 10°$ and still cross-cut the same interface deflections. Nevertheless, given the limitations imposed by the inherent resolution of the seismic data, the results are quite encouraging.

Two issues regarding the robustness of the solution shown in Fig. 10 need to be addressed. First, only three incoming wave fronts have been used to constrain the model, and, of these, two have an angular separation of only 5°. Calculation of the *a posteriori* covariance matrix shows that the model parameters are poorly constrained in the regions $x = -20$ to 10 km, $x = 220$ to 260 km and $x = 50$ to 80 km (bottom two interfaces only) relative to parameters in the other regions of the model. By including data from several other sources, model parameters will be better constrained. However, we should note that, as the sources become further out of plane, the 2-D ray-tracing scheme becomes less accurate. Fig. 11 shows the result of including data from the Mindanao and South East Indian Rise source regions in the inversion. These sources are approximately 14° and 31° out of plane respectively. Fig. 11(a) shows the ray coverage through the final model, which is greatly increased from that of Fig. 10(d). Accordingly, the *a posteriori* covariance matrix exhibits a reduction in the uncertainty of most model parameters, although the parameters near the endpoints of the interfaces remain poorly constrained. Correlations between parameter uncertainties also decrease, reflecting an increase in model resolution. Fig. 11(b) shows the final model with the same fault structure interpretation given in Fig. 10(e). The most noticeable change in the model is a slight reduction in the amplitude of its lateral features. Otherwise, there is very little difference and the structural interpretation remains the same. The rms data misfit reduction is about 62 per cent in this case compared to 78 per cent for Fig. 10(e), a decrease that reflects the use of out-of-plane sources in a 2-D algorithm.

Second, it was noted earlier that the use of the Amadeus Basin deep reflection model as a basis for the *a priori* model did not adequately account for the different velocity characteristics of the Musgrave Block. For instance, much of the exposed Musgrave Block consists of granulite grade facies that have a higher velocity than sedimentary rock. In fact, the average crustal velocity of our starting model is approximately 0.3 km s^{-1} less than that used by Lambeck & Burgess (1992) in their forward modelling of the same data. However, as we demonstrated with the synthetic tests, teleseismic data do not constrain the mean vertical structure. Tests with the velocity of the starting model increased by 0.3 km s^{-1} showed only minor changes in the amplitude of the lateral features, with the top interface intersecting the surface at some points and the undulations in the bottom interface increasing slightly. The

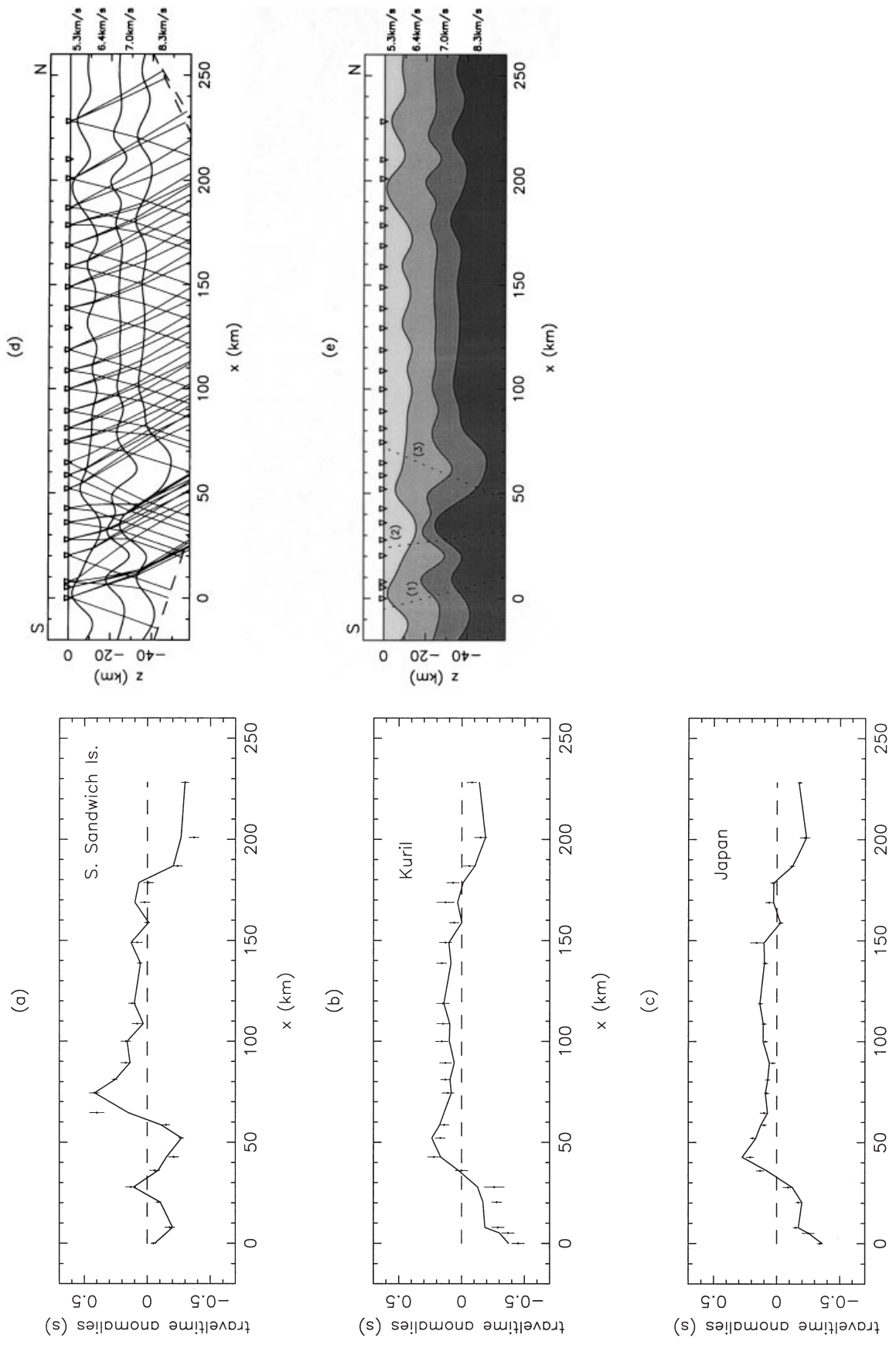

Figure 10. Inversion results for the Musgrave Line after nine iterations using data from three source regions. Comparisons between the travel time anomalies of the starting model (dashed line), final model (solid line) and observed values from McQueen & Lambeck (1996) (dots with error bars) are given for each of the three source regions: (a) South Sandwich Islands, (b) Kuril, and (c) Japan. (d) Ray coverage through the final model, and (e) final model with interpreted faults (dashed lines) corresponding to (1) Lindsay Lineament, (2) Wintiginna Lineament, and (3) Mann Fault.

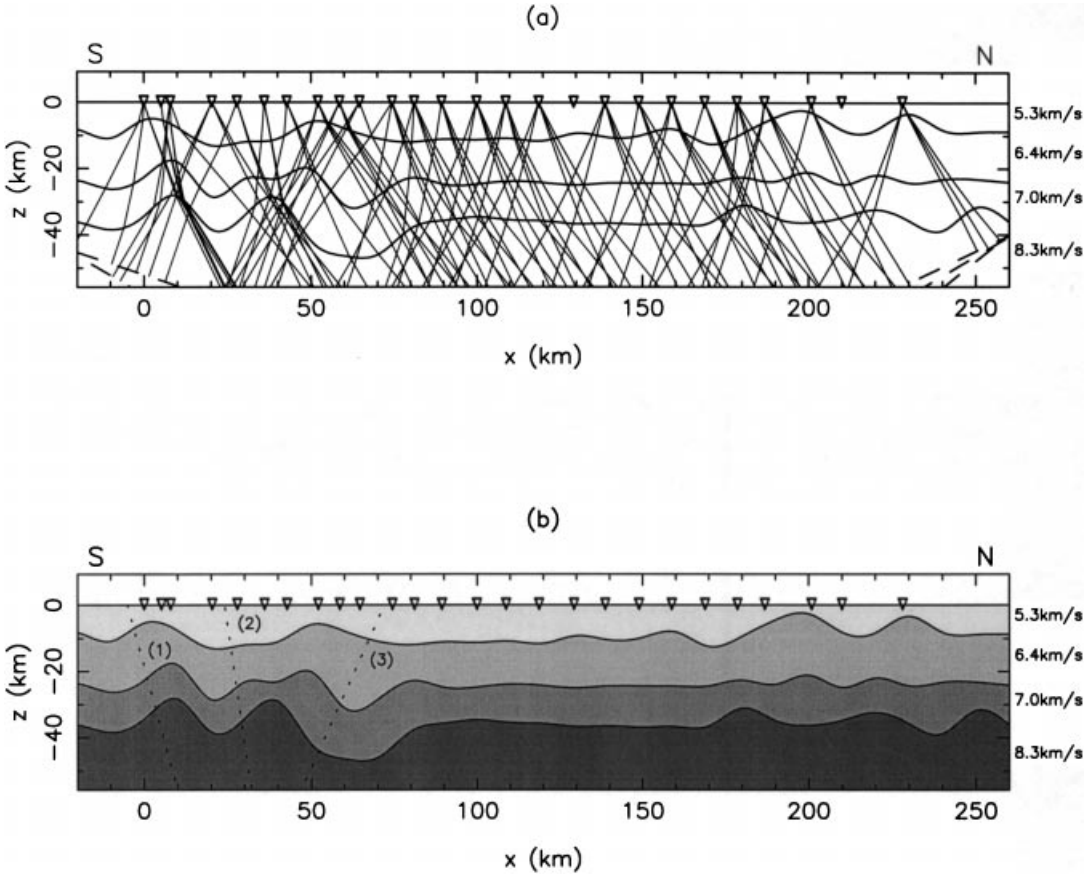

Figure 11. Inversion results for the Musgrave Line after six iterations using data (McQueen & Lambeck 1996) from five source regions (South Sandwich Islands, Kuril, Japan, Mindanao and South East Indian Rise). (a) Ray coverage through the final model, and (b) final model with the same interpreted faults (dashed lines) as Fig. 10(e).

increased amplitude of interface topography is to be expected since more variation in interface geometry is required if the velocity ratio across an interface is decreased. The important point is that the basic horizontal variation of the model is robust. Similarly, increasing the depth of the interfaces by between 4 and 7 km does not result in any marked change in lateral structure.

4 DISCUSSION

So far, it has been shown that the interface inversion method presented in this paper is capable of accounting for traveltime residuals by adjusting interface depth parameters rather than velocity parameters as is usually the case for teleseismic traveltime inversion. With the synthetic data, the target structure was known, so it was straightforward to see whether the inversion result was accurate or not. There is generally no independent check on inversion accuracy when real data are used (apart from the error and resolution estimates of linearized theory), but we can compare our central Australia model (Fig. 11) with the structures determined by other authors using the same data but different methods.

Lambeck & Burgess (1992) apply forward modelling to the same data set to determine crustal structure that is consistent with the data. Their model is defined by relatively few linear interface segments and contains an upper crust, lower crust, mantle and sediment layer, all with fixed velocities (see Fig. 12a). The modelling process they use: (i) allows for discontinuous interfaces and under/overthrusting of crust, (ii) traces rays through the 2-D structure in three dimensions and allows for diffractions, and (iii) attempts to fit the model to data from all available source regions. The most significant feature of their model is a steep southerly dipping thrust fault, corresponding to the Mann Fault, that results in a wedge of crust penetrating deeply (20–30 km) into the mantle. The secondary features of the model are two steep (even steeper than the main fault) northerly dipping faults corresponding to the Lindsay and Wintiginna lineaments. In the case of Fig. 11(b), the major structural feature is the steep dip on the deepest interface (Moho) at about $x = 50$ km. The same feature is echoed, but less prominently, in the upper interfaces. This structure has been interpreted (fault line 3) as the southerly dipping Mann Fault, and in this regard is consistent with the forward model of Lambeck & Burgess (1992). The interface inversion model does not show an underthrusting wedge of crust below the Mann Fault, but the large synform that pushes its way into the mantle is consistent with the approximation of such a structure by a smooth single-valued function. The orientation of the other two interpreted faults (1 and 2) also correlates well with those shown in the forward model.

McQueen & Lambeck (1996) apply inverse modelling techniques to the same data set to image the crustal structure. The

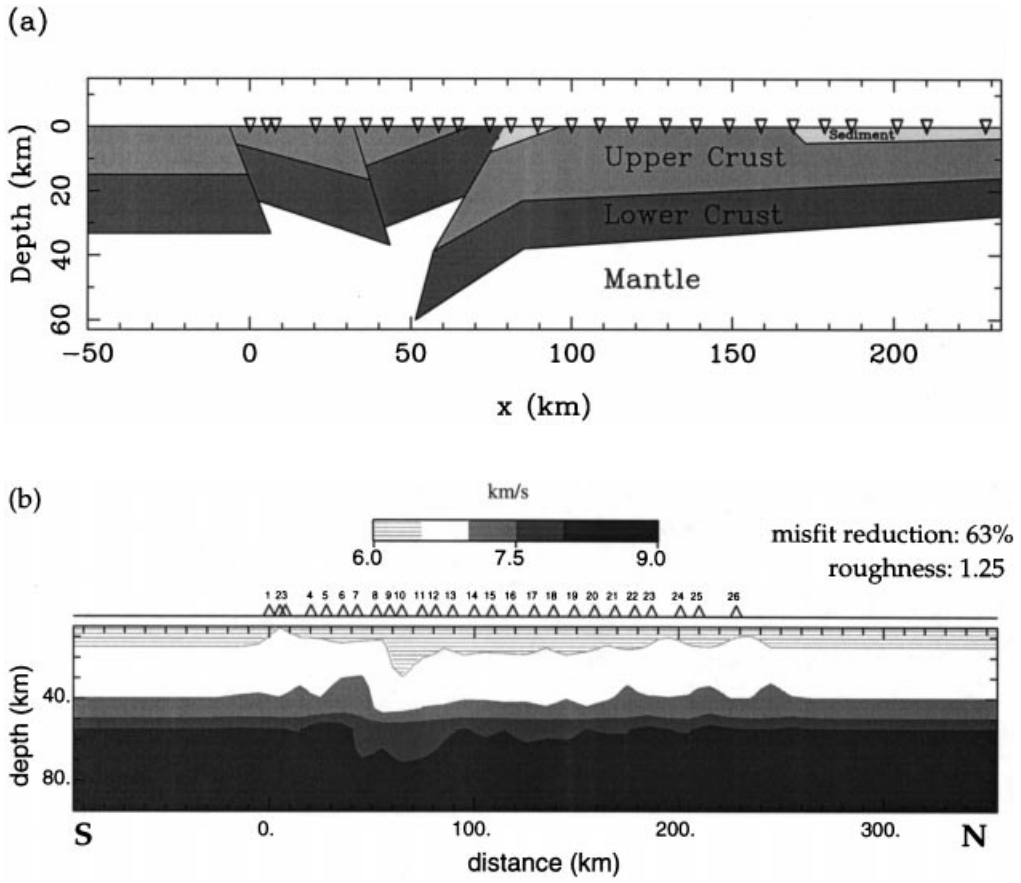

Figure 12. Models derived from the same data set using different methods. (a) Crustal structure obtained by forward modelling (after Lambeck & Burgess 1992) and (b) contours of velocity for the model obtained by inversion for slowness (from McQueen & Lambeck 1996).

inversion in this case is for slowness rather than interface structure, with the model parameters consisting of a grid of constant-slowness blocks. The slowness model produced by their inversion strongly indicates the presence of a southerly dipping fault in the approximate location of the Mann Fault. When this slowness model is superimposed onto a continuous 1-D background velocity model, a velocity section is produced (Fig. 12b). A direct comparison between this and Fig. 11(b) is complicated because McQueen & Lambeck's solution: (i) allows lateral structure to occur as far down as 90 km, (ii) uses a different background model to the initial model employed by the interface inversion model, (iii) traces rays through the 2-D structure in three dimensions, and (iv) has lateral structure indicated by isovelocity contours. However, the two solutions, one based on interface inversion, the other based on velocity inversion, are surprisingly similar in terms of lateral structure, with both models indicating a large low-velocity trough beneath the Mann Fault, with significant structure to the south but very little to the north ($x > 90$ km). Both inversions also suggest zones of higher velocity beneath stations 1–3 and station 26—these features correspond to known positive gravity lineaments. In addition, note that the rms data misfit reductions are almost identical for the two models: 62 per cent for Fig. 11(b) and 63 per cent for Fig. 12(b). The similarity of the two interpretations suggests that inversion for velocity and inversion for interface structure are alternative but equally valid ways of treating the data.

Another factor that needs to be considered with regard to our inversion method is the likely presence of lateral variations in velocity within a layer. In the model, these will manifest as errors in interface position. Velocity variations could explain some of the prominent features of the model, such as the large hump in the top interface at about $x = 200$ km, or the short-wavelength high-amplitude undulations in the bottom two interfaces between $x = 10$ and 40 km. Note that, in the latter case, these undulations are expected products of the model attempting to replicate the fault structures; the suggestion here, which indeed could be made about any other part of the model, is that lateral changes of velocity within a layer may have contributed to some of the model interface structure.

It is clear that using either a velocity-only model or an interface-only model means that the actual structure can only be approximated in the solution model. If we use a velocity model, interface structure will be mapped into velocity variation. Conversely, if we use an interface model, velocity variation will be mapped into interface structure. For example, in interpreting a velocity model, regions of high velocity could be caused by upward displacement of an interface separating low velocity over high; in interpreting an interface model, interfaces displaced upwards could be caused by locally high velocities in the layer above the interface. In principle, it is acceptable to use either type of parametrization if we bear this in mind. The data set from the Musgrave Line illustrates the difficulty of discriminating between structures that are best

characterized by continuous velocity variation and those that are best characterized by variable-thickness layers.

5 CONCLUSIONS

Inversion for interface geometry using teleseismic traveltimes represents an interesting and viable alternative to the usual approach of inverting for velocity structure. The relatively simple interface inversion method presented in this paper has been used to test this claim. The ray-tracing technique employed by the forward step of the method has proven to be quick and robust, and the conjugate gradient method used in the inversion was very effective in minimizing the objective function. Synthetic tests showed that the method could produce accurate results in the presence of realistic levels of data noise, and that lateral structure was recoverable even if layer velocities and initial interface positions were poorly chosen. The application of the method to real data collected in central Australia produced a solution that is consistent with previously published solutions that used the same data but different methods, most notably the approach that inverts for velocity rather than interface structure. Further work on the interface inversion method based on teleseismic data should include freeing up the parametrization to better represent features such as faults, allowing velocity gradients to occur within layers and extension to three dimensions.

ACKNOWLEDGMENTS

We thank Herb McQueen and Kurt Lambeck for kindly providing the central Australian teleseismic data set and Fig. 12(b). We also thank Malcolm Sambridge for his meticulous review of the original manuscript, which led to many improvements, and an anonymous reviewer for several constructive comments. All figures (except Figs 1, 3 and 12b) were generated using PGPLOT.

REFERENCES

Achauer, U., 1994. New ideas on the Kenya rift based on the inversion of the combined dataset of the 1985 and 1989/90 seismic tomography experiments, *Tectonophysics,* **236,** 305–329.

Aki, K., Christoffersson, A. & Husebye, E.S., 1977. Determination of the three-dimensional structure of the lithosphere, *J. geophys. Res.,* **82,** 277–296.

Benz, H.M., Zandt, G. & Oppenheimer, D.H., 1992. Lithospheric structure of northern California from teleseismic images of the upper mantle, *J. geophys. Res.,* **97,** 4791–4807.

Bishop, T.N., Bube, K.P., Cutler, R.T., Langan, R.T., Love, P.L., Resnick, J.R., Shuey, R.T., Spindler, D.A. & Wyld, H.W., 1985. Tomographic determination of velocity and depth in laterally varying media, *Geophysics,* **50,** 903–923.

Blundell, C.A., 1993. Resolution analysis of seismic P-wave velocity estimates using reflection tomographic inversion, *PhD thesis,* Monash University, Melbourne.

Bowman, J.R. & Kennett, B.L.N., 1993. The velocity structure of the Australian shield from seismic traveltimes, *Bull. seism. Soc. Am.,* **83,** 25–37.

Chiu, S.K.L., Kanasewich, E.R. & Phadke, S., 1986. Three-dimensional determination of structure and velocity by seismic tomography, *Geophysics,* **51,** 1559–1571.

Collins, C.D.N., 1988. *Seismic Velocities in the Crust and Upper Mantle of Australia,* Bur. Min. Resour., Aust., Bull., **277**.

Evans, J.R., 1982. Compressional wave velocity structure of the upper 350 km under the Eastern Snake River Plain near Rexburg, Idaho, *J. geophys. Res.,* **87,** 2654–2670.

Fletcher, R. & Reeves, C.M., 1964. Function minimization by conjugate gradients, *Comput. J.,* **7,** 149–154.

Herrin, E., Tucker, W., Taggart, J., Gordon, D.W. & Lobdell, J.L., 1968. Estimation of surface focus P travel times, *Bull. seism. Soc. Am.,* **58,** 1273–1291.

Hestenes, M. & Stiefel, E., 1952. Methods of conjugate gradients for solving linear systems, *Nat. Bur. Stand. J. Res.,* **49,** 409–436.

Hole, J.A., 1992. Nonlinear high-resolution three-dimensional seismic travel-time tomography, *J. geophys. Res.,* **97,** 6553–6562.

Hole, J.A., Clowes, R.M. & Ellis, R.M., 1992. Interface inversion using broadside seismic refraction data and three-dimensional travel time calculations, *J. geophys. Res.,* **97,** 3417–3429.

Humphreys, E.D. & Clayton, R.W., 1990. Tomographic image of the southern California mantle, *J. geophys. Res.,* **95,** 19 725–19 746.

Kosloff, D., Sherwood, J., Koren, Z., Machet, E. & Falkovitz, Y., 1996. Velocity and interface depth determination by tomography of depth migrated gathers, *Geophysics,* **61,** 1511–1523.

Lambeck, K., 1983. Structure and evolution of the intracratonic basins of central Australia, *Geophys. J. R. astr. Soc.,* **74,** 843–886.

Lambeck, K. & Burgess, G., 1992. Deep crustal structure of the Musgrave Block, central Australia: results from teleseismic travel-time anomalies, *Aust. J. Earth Sci.,* **39,** 1–19.

Lambeck, K. & Penney, C., 1984. Teleseismic travel time anomalies and crustal structure in central Australia, *Phys. Earth planet. Inter.,* **1984,** 46–56.

Lambeck, K., Burgess, G. & Shaw, R.D., 1988. Teleseismic travel-time anomalies and deep crustal structure in central Australia, *Geophys. J.,* **94,** 105–124.

Lindsay, J.F. & Korsch, R.J., 1991. The evolution of the Amadeus Basin, central Australia, in *Geological and Geophysical Studies in the Amadeus Basin, Central Australia,* pp. 7–32, eds Korsch, R.J. & Kennard, J.M., AGPS, Canberra.

Lutter, W.J. & Nowack, R.L., 1990. Inversion for crustal structure using reflections from the PASSCAL Ouachita experiment, *J. geophys. Res.,* **95,** 4633–4646.

McCaughey, M. & Singh, S.C., 1997. Simultaneous velocity and interface tomography of normal-incidence and wide-aperture seismic traveltime data, *Geophys. J. Int.,* **131,** 87–99.

McQueen, H.W.S. & Lambeck, K., 1996. Determination of crustal structure in central Australia by inversion of traveltime residuals, *Geophys. J. Int.,* **126,** 645–662.

Nowack, R.L. & Lyslo, J.A., 1989. Fréchet derivatives for curved interfaces in the ray approximation, *Geophys. J.,* **97,** 497–509.

Plumb, K.A., 1979. The tectonic evolution of Australia, *Earth Sci. Rev.,* **14,** 205–249.

Press, W.H., Teukolsky, S.A., Vetterling, W.T. & Flannery, B.P., 1992. *Numerical Recipes in FORTRAN,* Cambridge University Press, Cambridge.

Sambridge, M.S., 1990. Non-linear arrival time inversion: constraining velocity anomalies by seeking smooth models in 3-D, *Geophys. J. Int.,* **102,** 653–677.

Sambridge, M.S. & Kennett, B.L.N., 1990. Boundary value ray tracing in a heterogeneous medium: a simple and versatile algorithm, *Geophys. J. Int.,* **101,** 157–168.

Sato, T., Kosuga, M. & Tanaka, K., 1996. Tomographic inversion for *P* wave velocity structure beneath the northeastern Japan arc using local and teleseismic data, *J. geophys. Res.,* **101,** 17 597–17 615.

Tarantola, A., 1987. *Inverse Problem Theory,* Elsevier, Amsterdam.

Walck, M.C. & Clayton, R.W., 1987. *P*-wave velocity variations in the Coso region, California, derived from local earthquake travel times, *J. geophys. Res.,* **92,** 393–405.

Wang, B. & Braile, L.W., 1996. Simultaneous inversion of reflection and refraction seismic data and application to field data from the northern Rio Grande rift, *Geophys. J. Int.,* **125,** 443–458.

Wells, A.T., Forman, D.J., Ranford, L.C. & Cook, P.J., 1970. *Geology*

of the Amadeus Basin, Central Australia, Bull. Bur. Miner. Resour. Geol. Geophys., **100**.

White, D.J., 1989. Two-dimensional seismic refraction tomography, *Geophys. J.,* **97,** 223–245.

Williamson, P.R., 1990. Tomographic inversion in reflection seismology, *Geophys. J. Int.,* **100,** 255–274.

Zelt, B.C., Ellis, R.M., Clowes, R.M. & Hole, J.A., 1996. Inversion of three-dimensional wide-angle seismic data from the southwestern Canadian Cordillera, *J. geophys. Res.,* **101,** 8503–8529.

Zelt, C.A. & Smith, R.B., 1992. Seismic traveltime inversion for 2-D crustal velocity structure, *Geophys. J. Int.,* **108,** 16–34.